SCIENCE CHINA
Information Sciences

• RESEARCH PAPER •

December 2016, Vol. 59 122308:1–122308:10
doi: 10.1007/s11432-016-5585-x

Underwater sonar target imaging via compressed sensing with M sequences

Huichen YAN[1], Jia XU[2*], Xiang-Gen XIA[3], Xudong ZHANG[1] & Teng LONG[2]

[1]*Department of Electronic Engineering, Tsinghua University, Beijing* 100084*, China;*
[2]*School of Information and Electronics, Beijing Institute of Technology, Beijing* 100081*, China;*
[3]*Department of Electrical and Computer Engineering, University of Delaware, Newark, DE* 19716*, USA*

Received March 24, 2016; accepted April 27, 2016; published online August 9, 2016

Abstract Due to the low sound propagation speed, the tradeoff between high azimuth resolution and wide imaging swath has severely limited the application of sonar underwater target imaging. However, based on compressed sensing (CS) technique, it is feasible to image targets with merely one pulse and thus avoid the above tradeoff. To investigate the possible waveforms for CS-based underwater imaging, the deterministic M sequences widely used in sonar applications are introduced in this paper. By analyzing the compressive matrix constructed from M sequences, the coherence parameter and the restricted isometry property (RIP) of the matrix are derived. Also, the feasibility and advances of M sequence are demonstrated by being compared with the existing Alltop sequence in underwater CS imaging framework. Finally, the results of numerical simulations and a real experiment are provided to reveal the effectiveness of the proposed signal.

Keywords sonar, high-resolution imaging, compressed sensing, M sequence, coherence parameter, restricted isometry property

Citation Yan H C, Xu J, Xia X-G, et al. Underwater sonar target imaging via compressed sensing with M sequences. Sci China Inf Sci, 2016, 59(12): 122308, doi: 10.1007/s11432-016-5585-x

1 Introduction

Since 1970s, with the first patent on synthetic aperture sonar (SAS) issued in the United State [1], it has been developing along a similar path as synthetic aperture radar (SAR). Theoretically, both of them employ wideband waveforms to gain high-range resolution and use the synthetic aperture technique to obtain a large virtual aperture as well as a high azimuth resolution for far-range targets imaging [2–4]. Nevertheless, it is known that there is a tradeoff between high azimuth resolution and wide swath for synthetic aperture based imaging methods. Specifically, to obtain a high azimuth resolution and avoid Doppler ambiguity, the pulse repetition frequency (PRF) should be larger than the Doppler bandwidth. On the other hand, the PRF cannot be too large in order to obtain a wide swath and avoid the range ambiguity. With the increasing demands of both azimuth resolution and imaging swath, this tradeoff becomes more and more serious for modern SAS/SAR. Furthermore, this problem is even more severe for underwater SAS than SAR because the underwater sound wave propagation speed is much lower than

* Corresponding author (email: xujia@bit.edu.cn)

that of electromagnetic wave in space. As a consequence, the imaging results are much too blurred due to the long-period uncompensated random motion between successive pulses. For example, to image a target with only 75 m range spread, i.e., imaging swath, the PRF should be set 10 Hz approximately, which may obviously affect the Doppler imaging as well as the ultimate azimuth resolution. Hence the set of PRF is crucial there. On the other hand, the slow sound speed also reduces the efficiency of imaging. This problem has long been noticed, and since the illuminative work in early 1970s [5,6], along-track sensor array is adopted to increase the PRF physically. Motion compensation techniques [7] and phase gradient algorithm (PGA) [8], are applied to the raw data.

Compressed sensing (CS) [9–11] is a widely discussed technique for processing sparse signals. Despite few literature specifying CS imaging in sonar [12], CS based radar imaging methods have been proposed in many studies [13–19]. Among them, Ref. [13] proposed seminal work for one-dimensional imaging on range profiles, and CS was embedded into the convolution of the transmitted signal and the point targets. By designing the transmitted signal and subsampling the convolution result, the compressive matrix is built and an underdetermined equation is constructed. The follow-up work in SAR [14,15], inverse SAR (ISAR) [16], SAR tomography [17], ground penetrating radar (GPR) [18], through-wall radar imaging [19] and micro-Doppler analysis [20] is all based on this convolution framework. Adopting convolution-based CS approach, Ref. [21] extends to leverage direct recovery of the two-dimensional range-Doppler image. Also, the design of compressive matrix has been widely discussed in [22–27] with different waveforms. Furthermore, many effective CS reconstruction methods have been proposed for different scenarios [28–30].

In [21], CS provides a way to deal with the above tradeoff by forming the imaging problem into a linear equation when a target is formulated with a set of sparse scattering points. By meticulously transmitting the Alltop sequence as single probe signal, the compressive matrix is optimized for radar CS imaging and high-resolution target image can be reconstructed via single pulse. In real applications, diverse waveforms are necessary in military counter-surveillance, reconnaissance, anti-jamming, secret observations applications, etc. Therefore, in this paper the deterministic M sequence is introduced for CS-based sonar imaging based on the two-dimensional imaging scheme of [21]. Also, the advances of M sequence on the recovering errors are demonstrated by being compared with the Alltop sequence. In this paper, M sequences are adopted for CS two-dimensional imaging and the performance of M sequences is analyzed from the view of compressive matrix. In Section 2, the two-dimensional CS imaging is reviewed. In Section 3, the performance of M sequences is discussed in terms of compressive matrix. Numerical simulations and a real experiment are provided to demonstrate the effectiveness of the proposed method in Section 4. In Section 5, conclusion is drawn.

2 Two-dimensional CS imaging

The CS method is used to solve the linear problem,

$$\boldsymbol{y} = \boldsymbol{A}\boldsymbol{x}, \tag{1}$$

where $\boldsymbol{x} \in \mathbb{C}^n$ is a sparse unknown vector, $\boldsymbol{A} \in \mathbb{C}^{m\times n}$ $(m \ll n)$ is called the compressive matrix and $\boldsymbol{y} \in \mathbb{C}^m$ is the observation vector. If $\boldsymbol{A}$ is considered as a redundant basis, $\boldsymbol{y}$ is then the weighted sum of basis with weights $\boldsymbol{x}$.

In CS imaging framework, assume an imaging area of interest with $N \times N$ (N is a prime number) resolvable pixels in range Doppler plane with sparse point scatterers to be imaged. Each pixel represents a scatterer with certain range away from the sonar and Doppler caused by its radial velocity. This working mode resembles the inverse synthetic aperture (ISA) sonar. There the Doppler relates directly to the scatterer's azimuth position when a target is rotating around a specified axis uniformly. Therefore, the range-Doppler distribution may provide scatterers' strengths and positions in two-dimensional space in certain cases. The image can be written as a vector of $\boldsymbol{x}$ of length N^2 as in (1). To resolve N pixels in each dimension of the plane, we transmit an Alltop sequence of length N. For each of the N^2 pixels

with unit strength point scatterers, a unique echo will be generated. These normalized echoes, acting as columns, form an $N \times N^2$ basis as $\boldsymbol{A}$. With N samples as $\boldsymbol{y}$, a linear equation as (1) is thus constructed. We define the coherence parameter $\mu(\boldsymbol{A})$ of $\boldsymbol{A}$ as the maximum of the off-diagonal coefficient of the Gram matrix $\boldsymbol{G} = \boldsymbol{A}^{\mathrm{H}}\boldsymbol{A}$, or

$$\mu(\boldsymbol{A}) = \max_{1 \leqslant i < j \leqslant N^2} |\boldsymbol{G}(i,j)|. \tag{2}$$

In this case $\mu(\boldsymbol{A})$ approaches the Welch bound $1/\sqrt{N+1}$ [31], which optimizes the CS reconstruction performance. The restricted isometry property (RIP) [10] of $\boldsymbol{A}$ follows with an overwhelming probability.

3 CS imaging with M sequence

In the above $N \times N$ range-Doppler plane, let $N = 2^{\gamma} - 1$, γ is an integer. A periodic M sequence $s(n)$ with a cycle of N is transmitted with a modulation frequency f_{c} as

$$\begin{aligned} &f(t) = \frac{1}{\sqrt{N}} h(t) \exp(\mathrm{j}2\pi f_c t), \\ &\text{for } h(t) = s(n), \quad (n-1)\Delta < t \leqslant n\Delta, \quad n = 1, 2, \ldots, N, \end{aligned} \tag{3}$$

in one cycle, where Δ is the bit width of the M sequence, $\mathrm{j} = \sqrt{-1}$. Sound wave speed and wavelength are represented as c and λ, respectively. Suppose targets are sparsely distributed on the plane. By transmitting (3) for one cycle, for one particular scatterer as an example in the scene, we denote its range $R = pc\Delta/2$, Doppler $f_d = q(f_{\mathrm{c}}/N)$ $(p, q = 1, 2, \ldots, N)$, and backscattering strength as $\tilde{g}_{p,q}$. Its echo is demodulated and sampled with a frequency $f_{\mathrm{s}} = 1/\Delta$. With $2N-1$ samples obtained, we shift and add the last $N-1$ samples with the first $N-1$ samples, and then we can rewrite the first N samples of this scatterer's echo as

$$r_{p,q}(n) = g_{p,q} \cdot \frac{1}{\sqrt{N}} s(n-p) \exp\left(\mathrm{j}2\pi \frac{q}{N} n\right), \quad n = 1, 2, \ldots, N, \tag{4}$$

where $g_{p,q} = \tilde{g}_{p,q} \exp(\mathrm{j}4\pi R/\lambda)$ is a complex strength. Noticeably, to avoid disturbance, in the above process, it is assumed in this paper that all the scatterers of interest are sparsely distributed in the range of $1, 2, \ldots, N$ and no other strong scatterers are distributed in the range of $-N+1, -N+2, \ldots, 0$ or $N+1, N+2, \ldots, 2N-1$, which is fit for the imaging of an isolated underwater target. An alternative way to obtain (4) is to modulate multiple periods of M sequence, for example $s(1), s(2), \ldots, s(N), s(1), s(2), \ldots, s(N), \ldots$, on the continuous wave for transmission. Then Eq. (4) can be directly obtained from the second N samples of the received signal without the proposed shifting and adding operations. Eq. (4) shows one example of the echoes, and with the different combinations of p and q, there are N^2 such echoes in total. Just as Section 2, the backscattered signal $\boldsymbol{y}$ is the weighted summation of $r_{p,q}$, weighted by scatterers' strengths. Here we denote the compressive matrix as $\boldsymbol{\Phi}$. Matrix $\boldsymbol{\Phi} \in \mathbb{C}^{N \times N^2}$ can be divided into N square submatrices $\boldsymbol{\Phi}^{(k)} \in \mathbb{C}^{N \times N}$ $(k = 1, 2, \ldots, N)$ as

$$\boldsymbol{\Phi} = \left[\boldsymbol{\Phi}^{(1)} \middle| \boldsymbol{\Phi}^{(2)} \middle| \cdots \middle| \boldsymbol{\Phi}^{(N)}\right]. \tag{5}$$

Each submatrix in (5) tracks N different echoes of targets with different Dopplers and the same range,

$$\boldsymbol{\Phi}^{(p)}(n,q) = \frac{1}{\sqrt{N}} s(n-p) \exp\left(\mathrm{j}2\pi \frac{q}{N} n\right). \tag{6}$$

The strengths $g_{p,q}$ of the $N \times N$ pixels as (4) can be reshaped as a vector $\boldsymbol{x} \in \mathbb{C}^{N^2 \times 1}$, where many entries are zeros for a target with sparse scatterers. Then the sampled echo $\boldsymbol{y}$ can be rewritten as

$$\boldsymbol{y} = \boldsymbol{\Phi}\boldsymbol{x} + \boldsymbol{v}, \tag{7}$$

where $\boldsymbol{v} \in \mathbb{C}^{N \times 1}$ is the noise vector caused by thermal noise, basis mismatch and external interference, etc. Now the imaging problem is converted to the problem of reconstructing $\boldsymbol{x}$ by solving an underdetermined linear equation. To apply the CS-based method in (7), it is shown next in the theorem that matrix satisfies the requirements of CS.

Theorem 1. The coherence parameter $\mu(\boldsymbol{\Phi})$ satisfies

$$\mu\left(\boldsymbol{\Phi}\right)=\max\left|\boldsymbol{G}\left(i,j\right)\right|=\sqrt{N+1}/N, \tag{8}$$

for $1\leqslant i\leqslant N^2$, $1\leqslant j\leqslant N^2$, and $N=2^{\gamma}-1$.

Before proving Theorem 1, two lemmas are necessary to be introduced first.

Lemma 1. The number of -1 in an M sequence s in one period N is $\left(N+1\right)/2$ and that of $+1$ is $\left(N-1\right)/2$. Its N points cyclic autocorrelation can be given as

$$R_{\mathrm{s}}\left(n\right)=\begin{cases}N, & n=kN,\\ -1, & n=kN+l,\end{cases} \tag{9}$$

where $k\in\mathbb{Z},\ l=1,2,\ldots,N-1$.

Lemma 2. The XOR result of an M sequence of period N and its shift is still an M sequence of period N [32].

Proof of Theorem 1. The proof can be divided into 3 separate cases based on the selection of i and j. Without loss of generality, assume $i<j$.

Case 1. $kN<i<j\leqslant\left(k+1\right)N,\ k=1,2,\ldots,N$. It corresponds to the cases where the two columns are picked from the same submatrix of $\boldsymbol{\Phi}$. $\left|\boldsymbol{G}\left(i,j\right)\right|$ can be simply calculated by the sum of a geometric progression and we have $\left|\boldsymbol{G}\left(i,j\right)\right|=0$.

Case 2. $j-i=kN,\ k=1,2,\ldots,N$.

$$\left|\boldsymbol{G}\left(i,j\right)\right|=\frac{1}{N}\left|\sum_{n=0}^{N-1}s\left(\left\lceil\frac{i}{N}\right\rceil+n\right)s\left(\left\lceil\frac{j}{N}\right\rceil+n\right)\right|, \tag{10}$$

where $\lceil x\rceil$ represents the minimal integer that is greater or equal to x. The summation part in the right hand side of (10) is a cyclic autocorrelation of the M sequence $s(n)$. From Lemma 1, we have $\left|\boldsymbol{G}\left(i,j\right)\right|=1/N$.

Case 3. This corresponds to the cases where the two columns are picked from different submatrices with different Dopplers. In this case, we have

$$\left|\boldsymbol{G}\left(i,j\right)\right|=\frac{1}{N}\left|\sum_{n=0}^{N-1}s\left(n+l\right)s\left(n\right)\exp\left(-\mathrm{j}2\pi l\frac{n}{N}\right)\right|. \tag{11}$$

According to Lemma 2, $s_m\left(n\right)=s\left(n+l\right)s\left(n\right)$ is another M sequence in terms of n. Then, Eq. (11) can be reformulated as

$$\left|\boldsymbol{G}\left(i,j\right)\right|=\frac{1}{N}\left|\sum_{n=0}^{N-1}s_m\left(n\right)\exp\left(-\mathrm{j}2\pi l\frac{n}{N}\right)\right|. \tag{12}$$

Let S_m be the N-point DFT of s_m. Then, for $1\leqslant k\leqslant N-1$, we have

$$\left|\boldsymbol{S}_m\left(k\right)\right|^2=\left|\sum_{n=1}^{N}R\left(n\right)\exp\left(-\mathrm{j}2\pi\frac{k}{N}n\right)\right|=\left|\left(N+1\right)\exp\left(-\mathrm{j}2\pi k\right)\right|=N+1. \tag{13}$$

Consequently,

$$\left|\boldsymbol{G}\left(i,j\right)\right|=\frac{1}{N}\left|\boldsymbol{S}_m\left(k\right)\right|=\frac{\sqrt{N+1}}{N}. \tag{14}$$

It is shown that the coherence parameter of $\boldsymbol{\Phi}$ cannot approach Welch bound, but it can be asymptotic to the Welch bound when N increases. Matrices built from M sequences present nearly the same coherence property as Alltop sequences. It should be stated that some papers attempted to optimize the compressive matrix [26,27], but these results may not be applied in sonar scenario directly, while M sequence is a practically good choice. The coherence property and RIP can be tied up with Corollary 1.

Corollary 1. Matrix $\boldsymbol{\Phi}$ satisfies RIP of order K with the restricted isometry constant (RIC) $\delta_k = (K-1)\sqrt{N+1}/N$, for all $K < N/\sqrt{N+1}$.

To prove Corollary 1, Lemma 3 is presented first.

Lemma 3. The eigenvalues of an $M \times M$ matrix Ω, with entries $\omega_{i,j}$, $1 \leqslant i, j \leqslant M$, lie in the union of M discs $d_i = d_i(c_i, r_i)$, centred at $c_i = \omega_{ii}$, and with radius $r_i = \sum_{i \neq j} |\omega_{ij}|$ [5].

Proof of Corollary 1. Let $\Lambda \subseteq \{1, 2, \ldots, N^2\}$, with $|\Lambda| = K$ representing an index set, and $\boldsymbol{\Phi}_\Lambda$ is the submatrix of $\boldsymbol{\Phi}$, composed of the columns selected by indices in Λ. Consider the Gram matrix $\boldsymbol{G}_\Lambda = \boldsymbol{\Phi}_\Lambda^{\mathrm{H}} \boldsymbol{\Phi}_\Lambda$ with entry denoted as $\boldsymbol{G}_\Lambda(i,j)$, where $1 \leqslant i \leqslant K$, $1 \leqslant j \leqslant K$. From (6) and (14) we have for $i = j$,

$$\begin{aligned} \boldsymbol{G}_\Lambda(i,i) = \boldsymbol{G}(i,i) &= \left(\boldsymbol{\Phi}^{(p_i)}(:, q_i)\right)^{\mathrm{H}} \boldsymbol{\Phi}^{(p_i)}(:, q_i) \\ &= \sum_{n=0}^{N-1} \frac{1}{\sqrt{N}} s(n - p_i) \exp\left(-\mathrm{j}2\pi \frac{q_i}{N} n\right) \frac{1}{\sqrt{N}} s(n - p_i) \exp\left(\mathrm{j}2\pi \frac{q_i}{N} n\right) = 1, \end{aligned} \tag{15}$$

and for $i \neq j$,

$$\boldsymbol{G}_\Lambda(i,j) \leqslant \max |\boldsymbol{G}_\Lambda(i,j)| \leqslant \max |\boldsymbol{G}(i,j)| = \mu(\boldsymbol{\Phi}). \tag{16}$$

According to Lemma 3, if $K < N/\sqrt{N+1}$, $(K-1)\mu(\boldsymbol{\Phi}) < 1$ or $\boldsymbol{G}_\Lambda(i,j) \leqslant \boldsymbol{G}_\Lambda(i,i)$. Matrix $\boldsymbol{G}_\Lambda$ is positive definite, so the columns of $\boldsymbol{\Phi}_\Lambda$ are linearly independent and the eigenvalues of $\boldsymbol{G}_\Lambda$ are in the range of $[(1-(K-1)\mu), (1+(K-1)\mu)]$. Hence for arbitrary $\boldsymbol{x}$ with sparsity no greater than K, we have

$$(1 - \delta_K) \|x\|_2^2 \leqslant \|\boldsymbol{\Phi} x\|_2^2 \leqslant (1 + \delta_K) \|x\|_2^2, \tag{17}$$

with the RIC $\delta_K = (K-1)\sqrt{N+1}/N$.

Alternatively, the coherence can directly link to the recovery conditions. Corollary 2 illuminates the relationship between the scatterer number K, i.e., the signal sparsity, and the coherence, which is a direct result of Theorem B in [11].

Corollary 2. To image a sparse target with K scatterers in an $N \times N$ plane, if $K < \left(1 + N/\sqrt{N+1}\right)/2$, the target can be imaged by solving $\boldsymbol{y} = \boldsymbol{\Phi x}$ via basis pursuit (BP) or orthogonal matching pursuit (OMP).

In reality, noise cannot be overlooked. Corollary 3 states the relationship between the sparsity K and the coherence under noisy environment, which follows from Theorem 3 in [30].

Corollary 3. To image a target in an $N \times N$ plane with N samples when the noise $\|\boldsymbol{v}\| < \varepsilon$, if the number of scatterers of the target

$$K < \left(\sqrt{N+1}/N + 1\right) / \left(2\sqrt{N+1}/N + 4\varepsilon\sqrt{N}/T\right), \tag{18}$$

the target can be imaged with L1-norm error less than T, by solving the underdetermined Eq. (7) via basis pursuit denoising (BPDN).

Both Corollaries 2 and 3 guarantee the successful imaging of sparse scatterers by using M sequences via CS-based methods. As a remark, it should be noticed that a CS method assumes the target can be divided by grids in advance, while in reality, the scatterers may be distributed off the centres of the grids, and the SNR may be relatively low. Therefore, the off-grid scatterer imaging problem in low SNR with more diverse waveforms should be discussed in the future.

4 Numerical experiments for performance analysis

4.1 General discussion of the effectiveness of M sequence

In this section, four simulations and one experiment are made to demonstrate the effectiveness of M sequences. In the first simulation, a matrix $\boldsymbol{\Phi}$ is constructed with $N = 31$. The transmitted sequence is

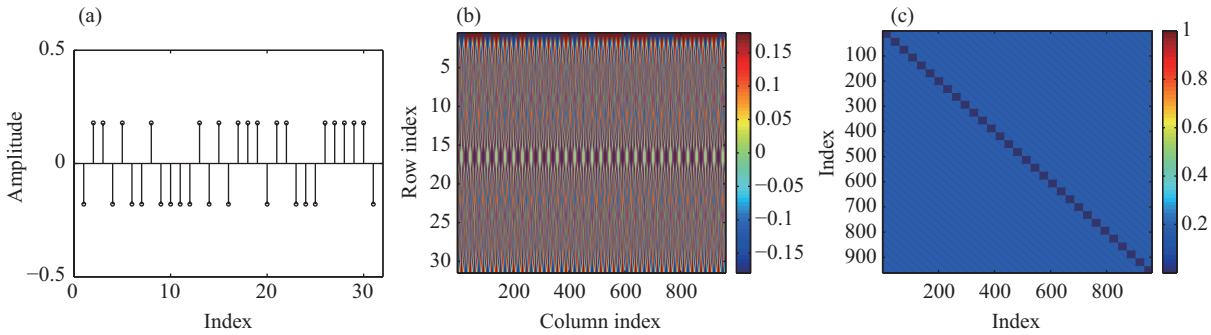

Figure 1 (Color online) An example of M sequence, its corresponding compressive matrix $\boldsymbol{\Phi}$ and Gram matrix of $\boldsymbol{\Phi}$. (a) An M sequence of length 31; (b) compressive matrix $\boldsymbol{\Phi}$ constructed from M sequence; (c) Gram matrix of $\boldsymbol{\Phi}$.

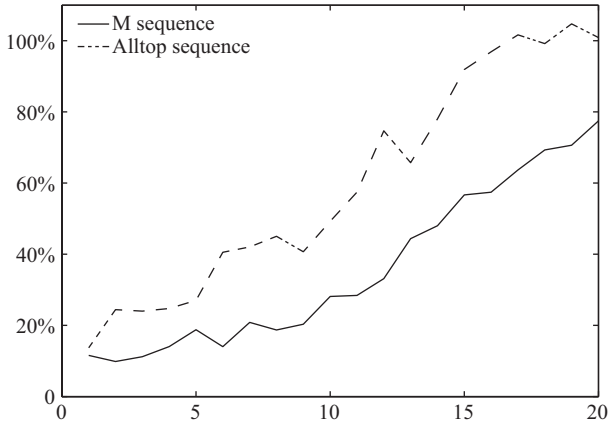

Figure 2 The average imaging relative errors of the two waveforms.

drawn in Figure 1(a), the real part of the matrix is shown in Figure 1(b) and its Gram matrix $\boldsymbol{\Phi}^{\mathrm{H}}\boldsymbol{\Phi}$ is in Figure 1(c). It is seen from Figure 1(b) the matrix $\boldsymbol{\Phi}$ inherits the randomness of an M sequence and Figure 1(c) is an intuitive explanation of Theorem 1.

In order to compare the imaging performances of M sequence and Alltop sequence, the relationship between the sparsity of the target K and the imaging accuracy is shown in the subsequent simulation. For each sparsity of K ranging from 1 to 20, scatterers with random distributions and strengths in the range-Doppler plane are generated given $N = 31$ with 100 trials. The average imaging relative errors (the imaging relative error refers to the ratio of error's L2-norm and the ground truth's L2-norm) of the two waveforms are plotted in Figure 2. In this simulation, no noise is added to the system, and BP is applied to solve the equation $\boldsymbol{y} = \boldsymbol{\Phi x}$. It is shown that error increases with the sparsity K. Besides, under the conditions indicated by Corollary 2, i.e., $K < 4$, the error is still not approaching zero. This is caused by outliers occurred with low probability during the recovery. It is interesting to notice that M sequence outperforms Alltop sequence under this situation. It is conjectured that in the Alltop sequence case, the correlations of different columns from different submatrices as (5) indicates are $1/\sqrt{N}$ uniformly, whereas in the M sequence case, parts of the coherences may be as low as $1/N$, thus lowing the error rate. In addition, the imaging error increases slowly when $K < 10$ in the M sequence case, indicating the bound in Corollary 2 is conservative in real applications.

4.2 Performance analysis with respect to target sparsity and dimensions

In the next simulation, the successful imaging rates are compared between the above two waveforms under different combinations of K and N. If we define the successful imaging as the cases where the relative L2-norm errors do not exceed 5%, in this simulation, the successful imaging rates are calculated for $N < 64$. For each K-N combination, 100 Monte Carlo trials are conducted, and the average errors are

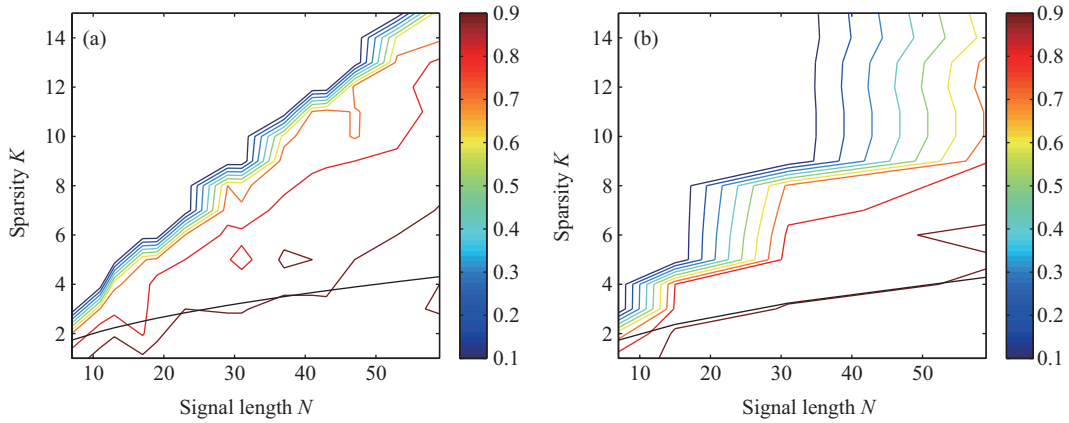

Figure 3 (Color online) Successful imaging rates of Alltop sequences and M sequences under different combinations of K and N. (a) Alltop sequence; (b) M sequence.

ploted. The results of M sequences and Alltop sequences are shown in Figure 3(a) and (b), respectively. The bound proposed in Corollary 2 is drawn in bold lines in the figures. It is seen that the bound is a conservative estimation. Furthermore, the successful imaging rate of the two waveforms performs almost the same. Alltop sequence drops dramatically when K increases. On the other hand, M sequence drops more slowly.

4.3 Performance analysis in noisy situations

In the next simulation, a sonar imaging scenario is simulated under different signal to noise ratios (SNR). In this case, SNRs are the ratios of the average signal energy to the average noise energy. An underwater target is generated with $K = 10$ scatterers in $N \times N$ square grids. An M sequence is transmitted with $\Delta = 0.1$ ms and $N = 31$. The sampling frequency is 10 kHz, and the imaging swath is around 4.65 m. The range resolution is 0.15 m with c =1500 m/s. The sample matrix is constructed as (5) and (6). According to Corollary 3, $K < 4$ is required for a successful imaging. However in the last experiment, Figure 3 indicates that it is possible under noisy situations to image the area with a greater K. In this experiment, the target is imaged by BPDN algorithm. Figure 4(a) shows the target of interest and Figure 4(b)–(d) gives the imaging result via CS with SNR ranging from 10 dB to 30 dB.

From Figure 4, it can be observed that the scatterers of target are composed of both strong and weak scatterers. When SNR=10 dB, the strong scatterers may be imaged successfully, whereas the weak scatterers are missing, and fake scatterers are generated. When SNR=20 dB, the phenomenon of fake scatterers and missing scatterers vanishes, yet the imaging result is still not accurate as amplitude error is obvious. When SNR=30 dB, the imaging result perfectly recoveries the target itself.

4.4 Real underwater experiment

In the last subsection, a real experiment is carried out to demonstrate the effectiveness of the proposed CS-based method. A ship model with length 1.2 m is rotating with a uniform angle velocity $\pi/2$ rad/s around a fixed spiale in the pool. The spiale is at the physical center of the model. Hence when the model is rotating, different parts on the model will have different speeds as well as Doppler frequencies. The further the point is with the center, the greater the speed. An M sequence with $N = 127$ is transmitted with signal bandwidth 100 kHz, modulated on a 5 MHz monotonic wave. The picture of the experiment is shown in Figure 5. The transducer is set in the upper right in the picture and the model is set in the lower left in the picture. The SNR of received echo is about 34 dB and the CS imaging result via the proposed method is shown in Figure 6. It is shown that the outline of the model can be recovered and the dense scatters can be recovered along the model. The picture shows a moment when the ship model's head is pointing to the sonar. Hence it spreads along the range direction. A bright point can be seen in the figure as the spiale in the middle of the model is made of medal, and it contributes to the result.

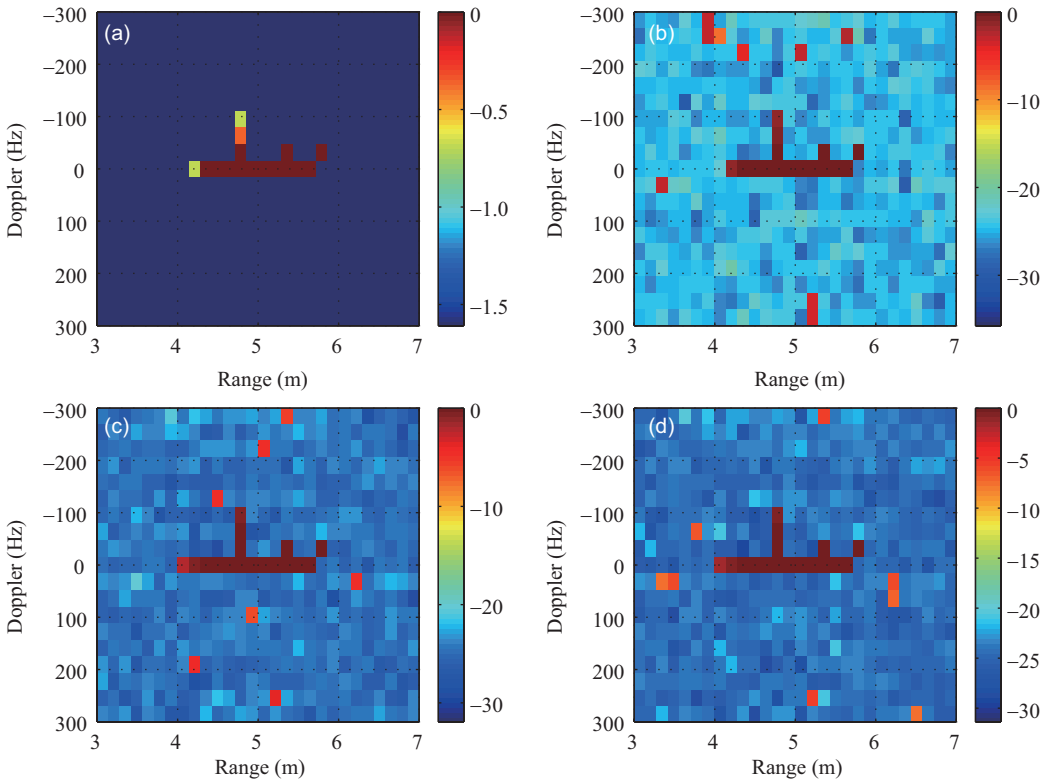

Figure 4 (Color online) A sonar imaging example. (a) Real target in the area; (b) imaging result (SNR=10 dB); (c) imaging result (SNR=20 dB); (d) imaging result (SNR=30 dB).

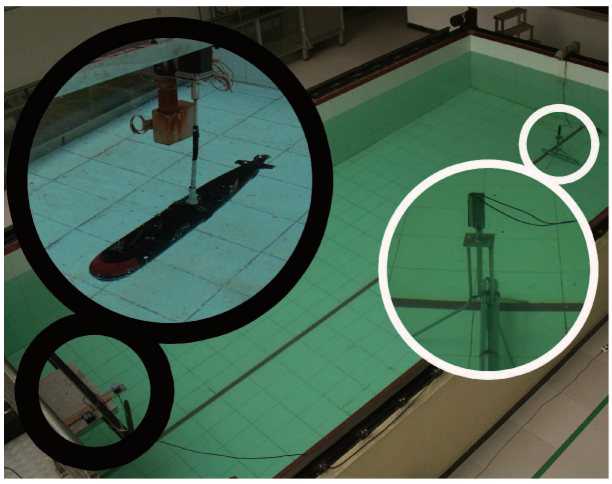

Figure 5 (Color online) The experiment layout.

5 Conclusion

Single pulse CS underwater imaging can provide a solution to the PRF design dilemma in synthetic aperture imaging and obtain high resolution and a wide swath, simultaneously. With the increase of code length of transmitting sequence, the imaging swath can be increased and the azimuth resolution can be improved accordingly. It is proven in this paper that an M sequence can be a candidate waveform for CS-based imaging, and it outperforms Alltop sequence with respect to the recovery errors. Finally, numerical simulation and an experiment are provided to demonstrate the effectiveness of the proposed method.

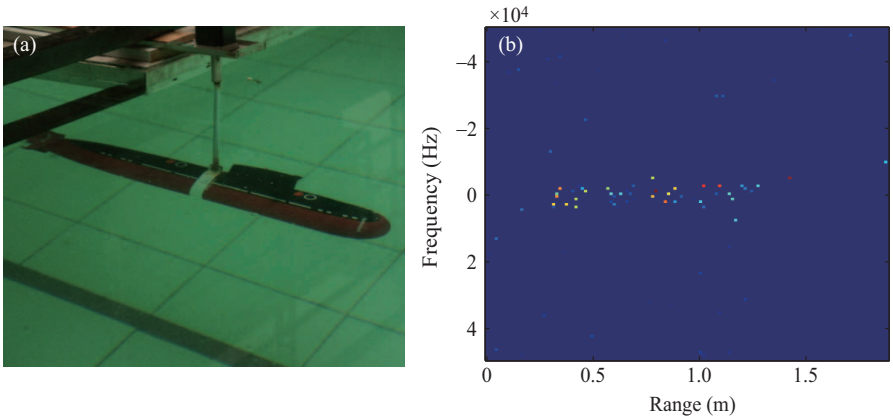

Figure 6 (Color online) The real experiment setup and result. (a) The ship model; (b) imaging result of the ship model.

Acknowledgements This work was supported in part by National Natural Science Foundation of China (Grant No. 61271391). 111 Project of China Ministry of Education (MOE) (Grant No. B14010), New Century Excellent Talents Supporting Plan of China MOE (Grant No. NCET-13-0049), Ministry Research Foundation (Grant No. 9140A21050114HT05338) and Outstanding Youth Teacher Training Plan of BIT (Grant No. BIT-JC-201205). The authors thank Professor Zhang Mingmin, and Doctor Lu Jianbin of Electronic Engineering College, Naval University of Engineering, Wuhan, China for their great supports in conducting the experiment.

Conflict of interest The authors declare that they have no conflict of interest.

References

1 Gilmour G A. Synthetic Aperture Side-Looking Sonar System. U.S. Patent 4088978, May 1978
2 Griffiths H D. Synthetic aperture imaging with sonar and radar: a comparison. In: Proceedings of the 5th World Congress on Ultrasonics, Paris, 2003. 511–518
3 Hayes P, Gough T. Synthetic aperture sonar: a review of current status. IEEE J Oceanic Eng, 2009, 34: 207–224
4 Franceschetti G, Lanari R. Synthetic Aperture Radar Processing. Boca Raton: CRC Press, 1999
5 Cutrona L J. Comparison of sonar system performance achievable using synthetic aperture techniques with the performance achievable with more conventional means. J Acoust Soc America, 1975, 58: 336–348
6 Cutrona L J. Additional characteristics of synthetic-aperture sonar systems and a further comparison with nonsynthetic-aperture sonar systems. J Acoust Soc America, 1977, 61: 1213–1217
7 Yu M, Xu J, Peng Y. Joint Doppler parameters estimation for squint-looking SAR. IET Radar Sonar Nav, 2007, 1: 207–212
8 Sutton T J, Griffiths H D, Hetet A, et al. Experimental validation of algorithms for high-resolution imaging of the seabed using synthetic aperture sonar. IET Radar Sonar Nav, 2003, 150: 78–83
9 Donoho D. Compressed sensing. IEEE Trans Inf Theory, 2006, 52: 1289–1306
10 Candes E, Romberg J, Tao T. Robust uncertainty principles: exact signal reconstruction from highly incomplete frequency information. IEEE Trans Inf Theory, 2006, 52: 489–509
11 Eldar Y, Kutyniok G. Compressed Sensing: Theory and Applications. New York: Cambridge University Press, 2012
12 Yan H C, Xu J, Xia X-G, et al. Wideband underwater sonar imaging via compressed sensing with scaling effect compensation. Sci China Inf Sci, 2015, 58: 020306
13 Baraniuk R, Steeghs P. Compressive radar imaging. In: Proceedings of IEEE Radar Conference, Boston, 2007. 128–133
14 Alonso T, Lòpez-Dekker P, Mallorquì J. A novel strategy for radar imaging based on compressive sensing. IEEE Trans Geosci Rem Sens, 2010, 48: 4285–4295
15 Yan H, Xu J, Peng S, et al. A compressed sensing method for a wider swath in synthetic aperture imaging. In: Proceedings of IET International Radar Conference, Xi'an, 2013. 1–6
16 Patel V M, Easley G R, Healy D M, et al. Compressed synthetic aperture radar. IEEE J Sel Top Signal Process, 2010, 4: 244–254
17 Zhu X, Bamler R. Tomographic SAR inversion by L1-norm regularization–the compressive sensing approach. IEEE Trans Geosci Rem Sens, 2010, 48: 3839–3846
18 Gurbuz A, McClellan J, Scott W. A compressive sensing data acquisition and imaging method for stepped frequency GPRs. IEEE Trans Signal Process, 2009, 57: 2640–2650
19 Li G, Burkholder R J. Hybrid matching pursuit for distributed through-wall radar imaging. IEEE Trans Antennas Propag, 2015, 63: 1701–1711
20 Li G, Varshney P K. Micro-Doppler parameter estimation via parametric sparse representation and pruned orthogonal

matching pursuit. IEEE J Sel Top in Appl Earth Observ and Rem Sens, 2014, 7: 4937–4948
21 Herman M, Strohmer T. High-resolution radar via compressed sensing. IEEE Trans Signal Process, 2009, 57: 2275–2284
22 Baraniuk R, Davenport M, DeVore R, et al. A simple proof of the restricted isometry property for random matrices. Constr Approx, 2008, 28: 253–263
23 Mendelson S, Pajor A, Tomczak-Jaegermann N. Uniform uncertainty principle for Bernoulli and subgaussian ensembles. Constr Approx, 2008, 28: 277–289
24 Tropp J A, Wakin M B, Duarte M F, et al. Random filters for compressive sampling and reconstruction. In: Proceedings of the IEEE International Conference on Acoustics Speech and Signal Processing (ICASSP), Toulouse, 2006. 14–19
25 Rauhut H, Romberg J, Tropp J. Restricted isometries for partial random circulant matrices. Appli Comput Harmon Anal, 2012, 32: 242–254
26 Xu J, Pi Y, Cao Z. Optimized projection matrix for compressive sensing. EURASIP J Advances in Signal Process, 2010, 43: 1–8
27 Cleju N. Optimized projections for compressed sensing via rank-constrained nearest correlation matrix. Appli Comput Harmon Anal, 2014, 36: 495–507
28 Tropp J. Greed is good: algorithmic results for sparse approximation. IEEE Trans Inf Theory, 2004, 50: 2231–2242
29 Donoho D, Elad M. On the stability of the basis pursuit in the presence of noise. EURASIP Signal Process J, 2006, 86: 511–532
30 Li K, Gan L, Ling C. Convolutional compressed sensing using deterministic sequences. IEEE Trans Signal Process, 2013, 61: 740–752
31 Welch L. Lower bounds on the maximum cross correlation of signals. IEEE Trans Inf Theory, 1974, 20: 397–399
32 Dinan E, Jabbari B. Spreading codes for direct sequence CDMA and wideband CDMA cellular networks. IEEE Commun Mag, 1998, 36: 48–54